Funct Neurol Rehabil Ergon 2013;3(2-3):275-293 ISSN: 2156-941X

ANATOMICALLY ACCURATE HEAD MODELS AND THEIR DERIVATIVES FOR DENSE ARRAY EEG SOURCE LOCALIZATION

Jasmine Song[1], Kyle Morgan[1], Sergei Turovets[*1,2], Kai Li[1], Colin Davey[1], Pavel Govyadinov[2], Phan Luu[1,3], Kirk Smith[4], Fred Prior[4], Linda Larson-Prior[4], and Don M. Tucker[1,3]*

[1]Electrical Geodesics, Inc., Eugene, OR USA
[2]Neuroinformatics Center, University of Oregon, Eugene, OR USA
[3]Department of Psychology, University of Oregon, Eugene, OR USA
[4]Electrical and Optical Imaging, Neuroimaging Laboratory, Washington University, St. Louis, MO USA

ABSTRACT

Electroencephalography (EEG) is a brain imaging technology that is noninvasive, cost effective, and provides millisecond temporal resolution. Improved spatial resolution of EEG measures can benefit multiple clinical and research applications, including the assessment of Traumatic Brain Injury (TBI), stroke, and neurodevelopmental disorders. Recent advances in electrode arrays have made it feasible to achieve dense array sampling (128, 256 and 512 channels) of brain potentials on the head surface, and then localize the sources of the measured fields to the surface of the cortex to provide spatially resolved information. Accurate dense array source localization requires i) moving beyond simplistic models of the human head (such as homogeneous multi-shell spheres) and ii) accurate knowledge of regional conductivities of head tissues. These requirements are particularly important for children because the size, shape and electrical properties of the head tissues undergo rapid developmental changes from infancy through adolescence. In this paper we apply high performance computing with finite difference methods (FDM) to solve the forward EEG problem with skull and head conductivity models that are appropriate for children as well as adults. We show that the improved structural (MRI and CT based) head models may improve high-resolution EEG source localization by correcting systematic biases in EEG source localization due to conductivity misspecifications and structural uncertainties. We also demonstrate how these same advances in electromagnetic head models may be used to model effects of non-invasive brain stimulation such as Transcranial Magnetic Stimulation (TMS) and Transcranial Electrical Stimulation (TES).

Keywords: EEG, pediatric, atlases, models, source localization, MRI, CT, SEP, mismatch

* Correspondence: Sergei Turovets, PhD, Electrical Geodesics, Inc., 1600 Millrace Dr. Suite 200. Eugene, OR, 97403, USA
E-Mail: sturovets@egi.com.

INTRODUCTION

Electroencephalography (EEG) provides important information on brain activity for a range of applications, including research on normal cognitive development in children, brain monitoring of neonates in intensive care, and early detection of brain pathology such as epilepsy. In adults, imaging technologies may use ionizing radiation (computed tomography (CT) or radionucleotides (positron emission tomography (PET), single photon emission tomography (SPECT), or they may require that the subject remains still during image acquisition (magnetic resonance imaging (MRI) or CT). In children, radiation exposure and sedation are particularly problematic. Better spatial resolution for the inexpensive and noninvasive EEG measure, such as through accurate source localization, could improve both research and health care [1]. A fundamental limitation to the use of source localization techniques lies in the relatively sparse sensor arrays used in standard EEG monitoring systems (19-21 electrodes in the standard 10-20 system). These conventional recording arrays provide inadequate spatial coverage [2] both in terms of the inter-electrode distances (~5 cm) and the coverage of basal regions of the head [3]. Many laboratories now acquire data from dense arrays of 64, 128, or 256 channels [4]. By increasing the spatial sampling of the volume and decreasing the inter-electrode distance, dEEG has been shown to provide a significantly improved spatial resolution from scalp recorded data [5].

At present, the use and validation of dEEG and Electromagnetic Source Imaging (ESI) in infants and children is hindered by the lack of accurate pediatric head models. To generate an ESI solution, two independently specified problems must be solved: (1) the forward problem, or volume conduction head model, which includes a set of conditions that specify the way in which currents propagate from their site of generation at the cortex to the site of measurement at the scalp, and (2) the inverse problem. The inverse problem requires mapping the recorded surface potentials to the cortical sources space in the volume conductor model, and this is a problem for EEG because it is highly underspecified. While many studies have shown that "realistic" volume conductor head models generate more accurate ESI solutions [2, 3, 6], the impact of the structural head tissue geometry, conductivity specifications, computability and necessity of additional variables such as tissue anisotropy or inhomogeneity remain poorly understood [7, 8]. These parameters are particularly critical for infants and children, where both shape and density of the skull and the structure of the cortex cannot be approximated by adult head models [9, 10].

The human skull and brain undergo rapid and significant growth from birth to about 2 years of age, with slower but continued growth through the 6th postnatal year [9-11]. Ossification of the skull begins at approximately 11 weeks gestational age [12] and is not fully complete until the 3rd to 4th decade of life [11]. While adult bone represents a layering of cortical (external and internal) and diploic bone, infant cranial bone (birth – 6 months of age) is primarily cortical bone [13]. This difference can be expected to lead to a significant change in skull resistivity from infancy to adulthood [14]. In addition, the developing skull exhibits large discontinuities, the fontanels (Figure 2a, 3a and 5 in this paper), which form at the intersection of 3 or more ossifying bone edges. These usually ossify over the first 2 years after birth, but the cranial sutures remain incompletely ossified at least until early adulthood. The open sutures and fontanels, as well as the unique shape of infant heads, must be modeled for accurate source localization [6 -8,18-23].

In addition to differences in the bony cranium, significant changes in brain volume, regional tissue composition and ventricular volume are seen in infants and children. The few imaging studies of normal brain development in children from birth to 2 years report that this is a period of significant dynamic micro- and macro-structural change [9,10]. During this period, brain volume increases 115%, lateral ventricular volume increases an amazing 288%, and white matter volume, a reflection of axonal myelination, increases substantially. This rapid growth trajectory is maintained into the 10th

year and is further reflected in differences in fractional anisotropy and mean diffusivity across the developmental period [15]. The importance of including age-specific regional brain anisotropy is not fully understood. The human brain exhibits large changes in regional anisotropy between the ages of 0-9, in addition to major changes in brain and tissue volumes from ages 0-2 that almost certainly are of critical importance to accurate modeling. In the course of creating accurate and useful pediatric head models, it would be useful to evaluate the age ranges in which changes in brain and tissue volume, in addition to regional anisotropies, significantly impact the accuracy of electrical source localization.

Several studies have addressed the issue of conductivity parameter misspecifications in adult head models including anisotropy and inhomogeneity. The effects of these parameters have been studied using analytic forward solutions in multi-shell spheres or MRI-based boundary element models (BEM) and finite element models (FEM) [18, 19, 38]. For example, Pohlmeier et al. [20] showed that by using an equivalent dipole approach (continuous dipole fit) one can obtain up to a 6 mm error increase with 20% skull misspecifications in both spherical and realistically shaped models. The uncertainty in the reported skull conductivity data range, in fact, can be up to a factor of 10. On the other hand, simulations by Huiscamp et al. [21] showed source localization error up to 20 mm for conductivity misspecification. More recently, Acar and Makeig [22] reported effects of forward model variation and mismatch on EEG source localization in adults using the BEM and equivalent dipole techniques. They compared models derived from subject specific MR images and models warped to digitized individual head shapes from the MNI adult atlases [24] as well as the best fit spherical models. The four-layer (warped to electrodes) MNI models were found to be the best approximations to the ground truth of the individual head models for four adult subjects. We are unaware of similar studies in children across the developmental spectrum, except the paper by Roche-Labarbe et al. [23] on neonatal head BEM simulations with structural variations (fontanels, the whole skull layer).

In our approach, the subject head model geometry is created through: (1) high-resolution segmentation of head tissues, (2) cortical ribbon surface extraction with topology correction (to insure a correct and continuous surface), and (3) tessellation of the cortical surface (for example, 1 cm squares) for dipole seeding. This detailed geometric model is then populated with the estimated conductivity for each tissue. At this point the *forward* model can be used to create the subject specific Lead Field Matrix (LFM) by individually activating each current dipole with unit magnitude and calculating the resultant scalp electrical potentials at the sensor locations. A complete formal description of the forward and inverse problems has been presented previously [1,27, 28, 40].

The structural changes that mark the development of the skull and brain are accompanied by changes in brain function and cognition [29]. While simple cognitive functions such as processing of sensory information and responses to sound and language are present at birth, the integration of higher order cognitive coordinating centers such as the prefrontal cortex show a protracted course of development [30]. Anomalies in the development of cerebral connections are relevant to a number of developmental disorders, including attention deficit hyperactivity disorder (ADHD), autism spectrum disorders (ASD) and schizophrenia (SZP). At least some of the characteristic features of these disorders have been attributed to disruptions in dynamic neural network interactions [31], a full elucidation of which requires neuroimaging with adequate temporal resolution. Although changes in network dynamics might be quantifiable using electrophysiological methods alone, the greatest benefit would derive from a clear definition of regional components of such networks. For that reason, accurate head models that would enable finer scale resolution of anatomical regions involved in network interactions using dEEG represent a much-needed tool. Furthermore, such head models would aid in the development of non-invasive multi-modal imaging by enabling the co-registration of age-specific anatomical images. This need, which is currently being addressed in adult populations, is particularly wanting in infants and children.

In this paper we conducted a simulation study based on Finite Difference Modeling (FDM) to examine the error when a rescaled or warped adult head model, an older child's head model, or inaccurate skull conductivities, are used in pediatric ESI. Specifically, we analyzed several pediatric head models based on: (1) the reference model, a 6 month old infant MRI co-registered with the infant's own CT; (2) the same MRI with warped adult CT atlas skull, with no fontanels but with adjusted thickness; (3) a child head model from a preschool age group warped to the 6 month old infant head shape; (4) a child head model from a teenage group warped to the reference infant head shape; and (5) an adult male head model warped to the reference infant head.

In contrast to previous studies, where a skull compartment was derived from MRI, we used the infant's or children's own CT in all models. The CT provides an excellent representation of bone structure and density of the skull, the most resistive tissue of the head and therefore having the largest impact in electrical modeling. All models have differentiated five tissue layers: scalp, skull, CSF, brain grey matter (GM) and white matter (WM), as well as internal air pockets in sinuses and throats.

The effects of geometry variations (such as the presence or absence of fontanels) and the skull conductivity variations were also examined systematically. All models were analyzed for six skull conductivity values, ranging from the lowest value reported in the literature 0.004 S/m through the average adult value 0.018 S/m to the average scalp conductivity (effectively no skull). The "synthetic ground truth" EEG was generated separately in each model for the "true" conductivity value. In the model mismatch studies, the ground truth EEG was generated in the reference infant model. Inverse solutions were examined in the true, warped, or modified models using minimum norm (MN) and sLORETA methods of distributed linear inverse source localization [8]. In addition, we examined the impact of different resolutions in medical images and FDM computation on ESI accuracy comparing the source localization results in the reference infant models for 0.5 mm, 1 mm, and 2 mm FDM resolutions. Finally, we illustrated the impact of model mismatch on source localization accuracy with a Somatosensory Evoked Potential (SEP) experiment with two adults. The mismatched models were created intentionally by warping or geometry swapping with a different subject's head model.

METHODS

All research retrospective and prospective protocols involving human subjects were approved by Institutional Review Boards (IRB) at both project sites (Eugene, OR and Saint Louis, MO), with informed consent obtained from the subjects recruited in the prospective studies. Figure 1 summarizes the head model creation, data collection, and model analysis path. Each of the steps starting with structural anatomical data and ending with source localization on cortex is outlined in Figure 1 and described in detail below.

MRI and CT data collection: The reference models of soft head tissues for adult subjects were derived from T1-weighted MR images of the heads of a 36-year-old healthy Asian male (subject A1) and two healthy Caucasian males: a 42-year-old (subject A2), and the Atlas Man (subject A0, also known as Colin27 at the MNI website [24]). The first two images were obtained with a 3T Allegra and the third with 1.5 T Magnetom Symphony scanners (Siemens Healthcare, Erlangen, Germany). The bone structure for these three subjects was derived from CT scans recorded with a GE CT scanner (General Electrics, Fairfield, United States). The acquisition matrix was 256 × 256 × 256 with a voxel size of 1mm × 1mm × 1mm in both the CT and T1 scans.

Retrospective pediatric CT and MRI data were acquired by data mining the clinical image repository of the Washington University BJC Health System in St. Louis, Missouri, United States. A query preparatory to research was conducted against a system that indexes Radiology reports [37]. This initial query identified 174,000 possible pediatric records. The more focused search on recent years 2006-2012 and based on the search string "CT+MR+CH (Children's Hospital)" was submitted

to the repository and yielded 11,000 potentially useful cases. Based on an initial sampling of this data, we predicted a 5% acceptance rate of data appropriate for constructing pediatric head models. An additional search term indicating head/brain (CT + MR + brain + head + CH) resulted in a total 2,500 exam reports. Search criteria were iteratively refined by review of radiology report text for actual presence of both MRI and CT scans, and by no more than a 6 month time interval between the two scans. As a result, 385 subjects were selected for retrieval and visual examination using a research PACS (Philips Healthcare, Andover, MA). Exclusion criteria were further refined through visual inspection for gross anomalies, resulting in data for 131 subjects being selected, de-identified, and entered into the study. Further reduction in the subject population occurred during morphometric analysis and visual inspection due to factors such as clipped field of view and subtle motion artifacts. Ultimately a total of 63 usable pediatric subjects (covering the age range between 0 to 18 years old) were entered into analysis. This represents 16% of the 385 subjects that passed initial screening or 0.04% of the initially identified potential subjects available in the clinical repository.

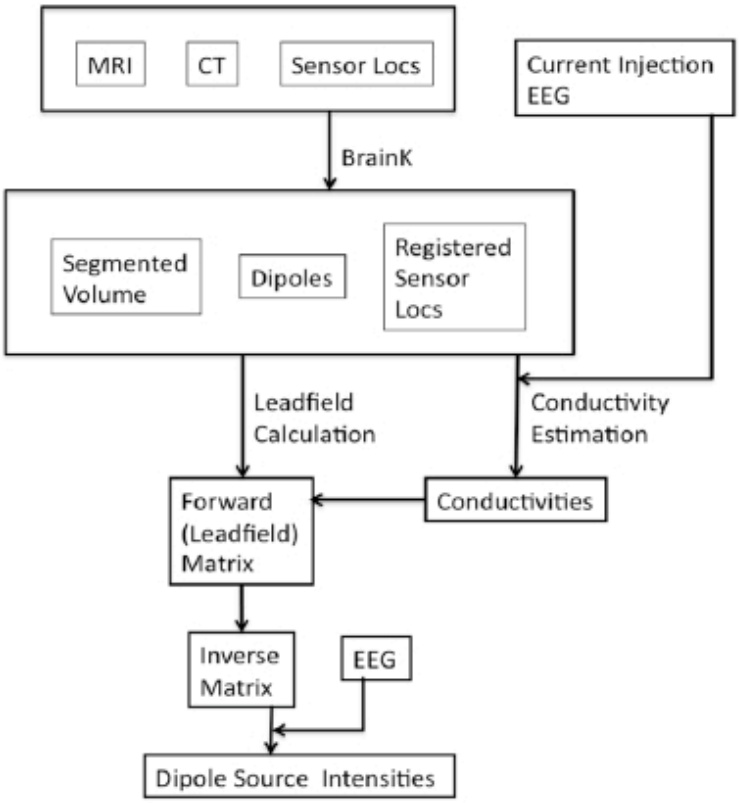

Figure 1. The diagram showing the data and workflow in source localization. MRI and CT may be subject-specific or warped from atlases. Sensor locations may be also subject-specific from Geodesic Photogrammetry System [36], or based on average sensor locations. Conductivities may be estimated [28] or values from the literature may be used. Lead fields calculation performed with FDM (this paper) or other known methods (FEM, BEM) [7]. Inverse matrix may be one of the published methods, e.g.: Minimum Norm, LORETA, sLORETA and LAURA [8].

Somatosensory EEG data collection experimental paradigm and recording: Two adult male subjects (A1 and A2) were positioned in a comfortable chair with their feet flat on the floor and rested their head on a chin-rest to avoid head movement artifacts. Each participant was instructed to remain relaxed and refrain from blinking as much as possible while staring at a fixation point throughout the

EEG recording. Digit I of the left and right hands were stimulated individually using a custom-made piezo-electric stimulator. During the recording, the piezo was lightly taped to the digit of interest, and the participant's hand was placed between two cotton towels to muffle the "tap" sound created by the stimulator. The stimulations were segmented into blocks in which each digit was stimulated at a rate of 2Hz for 200 seconds, resulting in 400 trials per block. Each digit was stimulated for one block before the tapper was moved to the other hand, and then was moved back once, resulting in 4 staggered blocks and 800 trials per digit. EEG was acquired using a 256-channel array EGI EEG 300 system and sensor positions were determined using the Geodesic Photogrammetry System (GPS) [36].

Head Model Construction: To build anatomically accurate head model geometry, the T1 MRI images were automatically segmented into seven tissue types (brain gray matter, brain white matter, CSF, scalp, eyeballs, air and skull), and then the CT images were coregistered (or warped) to the MRI using EGI's segmentation and image processing package, BrainK [32,33]. BrainK is a set of automated procedures for characterizing the tissues of the human head from MRI, CT, and photogrammetry [36] images. BrainK achieves five major tasks: (1) image segmentation, (2) registration of head model components (MRI, CT, and EEG sensor positions from Geodesic Photogrammetry), (3) cortical surface extraction, (4) tessellation of the cortical surface for oriented dipoles, or generation of dipole triples on the gray matter grid, and (5) Talairach transformation (not used in the present analyses). BrainK MRI segmentation recognizes the white matter (WM) and the gray matter (GM). It partitions these into two hemispheres and it differentiates cerebellum from cerebrum. In addition, an entire head mask and the two eyeballs are recognized as well in the segmentation component. The eyeballs are important for the electrical head model because of the large far fields generated by their cornea-retinal potentials.

In the development of BrainK, Li [32] introduced a novel Relative Thresholding (RT) method for accurate tissue segmentation in the presence of MRI field inhomogeneity. Given the results of RT performed on a region of interest (ROI), BrainK also implements a novel sophisticated morphological image analysis (SMIA) technique and a cell complex based morphometric image analysis (CCMIA) method for white matter extraction, gray matter extraction, scalp extraction, and, topology correction of the cortical surface mesh. BrainK uses *a priori* knowledge (including structural, geometrical, and morphological observations on the neuroanatomy, and radiological observations on the structural imaging) to enable automated, accurate, and fast segmentation (performed by a trained technician in 20-30 minutes).

Once the initial tissue segmentation has been conducted, there are several workflow paths that can be chosen based on the available subject specific data. Each workflow scenario represents a different way in which a skull can be registered. For example, the scenario *Atlas to MRI* is used when an individual CT scan is unavailable but an individual T1 MRI is. In this scenario, an adult atlas skull will be registered to the MRI geometry and will act as a guide for bone placement within the head. Due to the developmental differences in skull geometries in infants (i.e. presence of fontanels), an individual CT is always preferred. In this study, the workflow *CT to MRI* was used to generate all subject specific head models; a scenario that takes a subject's own CT and warps it to the geometry defined in the MRI. In all scenarios, when the skull registration is conducted, the resulting head segmentation includes the following tissue types: WM, GM, CSF, bone, flesh, eyeball and air, in which the WM and the GM are further partitioned into two cerebral hemispheres and the cerebellum (Figure 2a).

For all workflow scenarios, following skull registration, a generic Geodesic Sensor Net spherical sensor cloud is warped onto the head contour of the subject. For the scenarios of *Atlas to MRI*, *MRI to CT*, and *CT to MRI*, an additional sensors-to-head registration procedure is conducted to register the EEG sensor position cloud onto the head surface using several fiducial landmarks. For the scenario *Atlas to EEG sensors*, an individual sensor cloud from Geodesic Photogrammetry acts as a template

for which any given head model warps to the physical positions of the sensors measured with photogrammetry. This allows users to rescale a generic head model atlas to the individual's actual head shape. A head model (one that has a full brain segmentation and skull registration) is required to be completed before sensor transformation can be accomplished.

After sensor registration, dipoles are allocated in two modes: *oriented* or *triples*. If the individual's MRI is available, the cortical surface is extracted, tessellated into patches, and an oriented dipole is fitted to the vector sum of the normals of all the triangles in the surface mesh of each patch, thereby describing an equivalent dipole model for that surface patch. If the individual's MRI is not available, then triple dipoles (fitting x, y, z components of the unknown orientation) are distributed evenly throughout the cortical gray matter of an atlas brain on a regular grid with a user specified spacing (typically 7 mm or 5 mm).

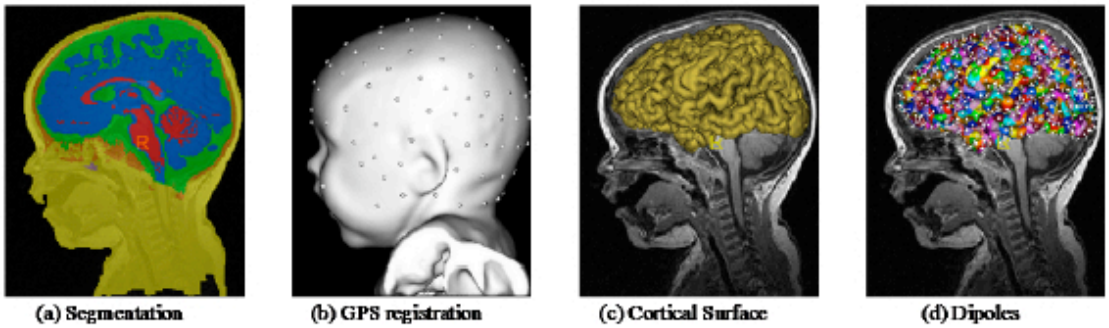

Figure 2. (a) BrainK Segmentation and CT to MRI coregistration differentiating scalp, skull, CSF, GM and WM in model C1 (a 6 month old subject). (b) A 128 sensor net registered on the same infant head. (c) Cortical surface generated. (d) Oriented dipoles set assigned to each cortical.

Forward Problem: The relevant frequency spectrum in EEG and MEG is well below 1 kHz, and most studies deal with frequencies between 0.1 and 70 Hz. Therefore, the volume conduction in EEG/MEG can be well described by the quasi-static approximation of Maxwell's equations, the Poisson equation. The electrical forward problem can be stated as follows: given the positions, orientations and magnitudes of current sources, as well as geometry and electrical conductivity of the head volume Ω calculate the distribution of the electrical potential on the surface of the head (scalp) Γ_Ω. Mathematically, it means solving the linear Poisson equation [7]:

$$\nabla \bullet (\sigma \nabla \phi) = S, \text{ in } \Omega \tag{1}$$

with no-flux Neumann boundary conditions on the scalp:

$$\sigma(\nabla \phi) \bullet n = 0, \text{ on } \Gamma_\Omega . \tag{2}$$

Here $\sigma = \sigma_{ij}(x,y,z)$ is an inhomogeneous tensor of the head tissues conductivity and $S = -I\,\delta(r-r_+) + I\,\delta(r-r_-)$ is the source current configuration constructed in the simplest case from a source and a sink of strength I at the vector locations r_+ and r_-. Having computed potentials $\phi(x,y,z)$ and current densities $J=-\sigma(\nabla\phi)$, the magnetic field B can be found through the Biot-Savart law. In this paper, we do not consider anisotropy or capacitance effects (the latter because the frequencies of interest are too small), but they can be included in a straightforward manner. Eq. (1) becomes complex-valued, and complex admittivity should be used [7, 38].

Lead Fields Calculations and Numerical Implementation: Lead Fields are defined as forward projections of unit strength dipoles' potential fields from cortex to scalp sensors. It is a matrix with the dimension: number of sensors (typically 256 or 128) by number of dipoles (typically 2400). The EEG session specific LFM requires a session specific set of sensor coordinates. A generic LFM for a given subject head volume can be calculated for more dense coverage of scalp (several thousand points) and then potentials for session specific sensor locations interpolated from this generic LFM on scalp. It can be accomplished by the "brute force" approach launching separately the forward solver for each dipole position. However, one can reduce the required number of forward solutions drastically by using the reciprocity principle for LFM calculations [7, 38, 40]. We have implemented both these approaches as they can be parallelized effectively in a multi-core cluster environment or desktops with modern Graphic Processing Units (GPUs: http://www.gpgpu.org/).

To solve Eq. (1) numerically we built a finite difference forward problem solver for the volume conduction based on the multi-component alternating directions implicit (ADI) algorithm [27,28, 40]. The numerical method is a generalization of the classic ADI algorithm, but with improved stability in 3D. We chose the FDM approach over FEM and BEM methods for its simplicity of implementation from the MRI/CT tissue segmentation map that produces a cubed lattice of nodes. Therefore, meshes are easy to construct (once segmentation is accomplished) as the cubic/rectangular elements can be mapped directly from the voxels of the medical images (3D MRI/CT scans), including all relevant anatomical details (in contrast to BEM and FEM).

To set up the boundary conditions in the heterogeneous biological media within a complex geometry like the human head, the method of the embedded boundaries is used in FDM. Here an object of interest is embedded into a cubic computational domain with extremely low conductivity values in the external complimentary regions. This effectively guarantees there are no current flows out of the physical area (the Neumann boundary conditions, Eq. (2), is naturally satisfied). The forward computations using high resolution structural models and the inverse conductivity search, which is composed of multiple forward solutions, represent computationally intensive tasks and require high performance computing. The electrical forward and inverse conductivity optimization models have been implemented in a parallel C/C++ code (OpenMP and MPI) and CUDA to run on multi-core cluster and GPGPU platforms [27,40].

EEG Source Localization: Estimating the source of EEG with distributed source models consists in first, allocating a grid of unit strength dipole sources with fixed locations and orientations in the whole brain volume or on the cortical surface, computing LFM for this dipole set, and then, estimating inverse solution for amplitudes of dipoles on this grid using the computed LFM and the scalp EEG data. For fixed positions and orientations, at a given time, the relation between source moments and the data can be stated as:

$$\Phi = KJ + \varepsilon, \tag{3}$$

where $\Phi \in {}^{\circ}{}^{N_e \times 1}$ is the electric potential; $J \in {}^{\circ}{}^{N_j \times 1}$ is the (unknown) amplitude and orientation of source distribution; $K \in {}^{\circ}{}^{N_e \times N_j}$ is the lead field matrix linking the current sources to the electric potential; $\varepsilon \in {}^{\circ}{}^{N_e \times 1}$ is the additive noise component (perturbation); N_e is the number of electrodes; N_j is the size of source distribution; N_d is the number of dipoles.

Estimating the source amplitudes consists in solving this noisy linear system. Considering the physics of data formation in EEG, source estimation is ill-posed ($N_e = N_j$). For a given data set, there is no unique source distribution. Further, after discretizing to a limited number of sensors, the corresponding K operator is ill conditioned, thus the solution is highly sensitive to small perturbations

in data and the model. This problem belongs to the linear ill-posed inverse problems. Methods for solving this problem, called inverse procedures, must take regularizing schemes into account to prevent the oscillatory behavior of the solutions in presence of noise.

The basic regularization methods range from constrained Minimum Norm (MN) [2-5,8] to minimization of regularized least-square cost functions such as:

$$\hat{J} = \arg\min_{J} \left\{ \left\| \Phi - KJ \right\|^2 + \alpha L(J) \right\},$$

where α is a positive scalar that is called the regularization parameter, and balances the data fidelity term $\left\| \Phi - KJ \right\|^2$ and prior term $L(J)$; $\left\| \bullet \right\|^2$ represents the square of the l_2-norm. The prior regularization operator $L(J)$ contains the priors that one wishes to take into account. For example, this operator can be taken in the form of the identity operator, which produces solutions with a minimum norm (MN), the gradient or weighted Laplacian operators (LORETA), local autoregressive average (LAURA), cortical surface laplacian (CSL), l_1-norm of the source amplitudes. In this paper, the MN and sLORETA [8] methods for the EEG inverse problem are used. The analytic solution for the MN method is $\hat{J} = K^T \left[KK^T + \alpha I_{N_e} \right]^{-1} \Phi$. The sLORETA solution is following: $\hat{J}_l^* = \left[C_{\hat{J}} \right]_{ll}^{-1/2} \hat{J}_l$, where $\hat{J}_l$ is the current density estimate at the l^{th} dipole and $\left[C_{\hat{J}} \right]_{ll}$ is the l^{th} diagonal of

$$C_{\hat{J}} = K \left[KK^T + \alpha I_{N_e} \right]^{-1} K$$

for $l = 1, \ldots, N_j$.

The distributed inverse problems can be divided into two scenarios. Scenario 1 (triple dipoles) estimates an unknown current density distribution, including both orientations and amplitudes of the source distribution. Scenario 1 assumes $N_j = 3N_d$ and $K \in \mathbb{R}^{N_e \times 3N_d}$ in Eq. (3). The root mean square (RMS) $R = \left[R_1, \ldots, R_{N_d} \right]^T \in \mathbb{R}^{N_d \times 1}$ is defined as $R_i = \sqrt{\left(J_{i,x}^2 + J_{i,y}^2 + J_{i,z}^2 \right) / 3}$, where $J = \left[J_1, \ldots, J_{N_d} \right]^T \in \mathbb{R}^{N_j \times 1}$, $J_i = \left[J_{i,x} J_{i,y} J_{i,z} \right]^T \in \mathbb{R}^{3 \times 1}$, for $i = 1, \ldots, N_d$.

Scenario 2 (oriented dipoles) estimates only unknown amplitudes of the source distribution given known orientations of dipoles. Since Scenario 2 assumes $N_j = N_d$ in Eq. (3), there is no need in calculation of RMS.

RESULTS

Model Warping

Several head models based on 3 original retrospective pediatric MRI/CT volumes (C1, C2, C3), and 3 prospective adult MRI/CT volumes (A0, A1 and A2) were created (see Table 1). The pediatric models represent the most distinct developmental age clusters [37]: infants 0 – 2 years old (C1), preschoolers 2- 6 years old (C2) and school age children 6 – 17 years old (C3). In most studies presented here, an infant model (C1, see Figure 2) for a 6 month-old was chosen as the ground-truth reference model. It was compared with derivative models from a preschooler pediatric model (C2) (6

years old), a teenager head model (C3) (14 years old), and an adult model (A1) to assess the effects of head model mismatch on source estimation results. The notations for those rescaled models (warped to the physical size of C1, but retaining the original morphology and having LFMs recalculated) are: C2', C3', A1' (see Table 2). We also created a 6 month old model with only the adult skull atlas (A0) warped and adjusted by thickness to match subject C1's specific MRI (notation A0s) and an adult mismatched model (A2 warped to A1, A2'). In all cases of warping the older age models to the reference infant model C1 the fontanel structure was lost (see Figure 3).

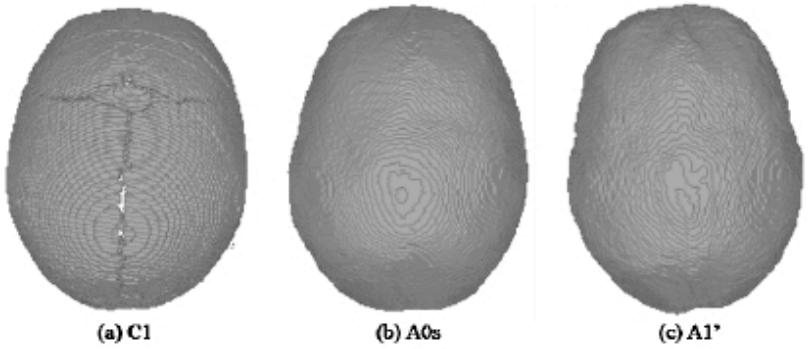

Figure 3. Skulls of three typical geometries. (a) The reference infant model C1 contains frontal and occipital fontanels. (b) Skull of the warped model A0s (only skull of A0 warped and adjusted to C1 MRI). (c) Skull of the warped model A1' (the whole adult head rescaled to the infant size). Notice that warped models have no fontanels.

Table 1. The original human subject models

	C1	C2	C3	A0	A1	A2
Age (years)	0.5	6	14	NA	36	42
Gender	NA	NA	NA	M	M	M
Original MRI/CT	yes	yes	yes	yes	yes	yes

Table 2. Derivative head models

	C2'	C3'	A1'	A2'	A0s
Warped Target Model	C1	C1	C1	A1	C1
All Tissue Warped	Yes	Yes	Yes	Yes	No (skull only)
Average Literature Values for Tissue Conductivity	Yes	Yes	Yes	Yes	Yes
Derivative LFM	Yes	Yes	Yes	Yes	Yes

The quality of the warping process can be evaluated based on the data presented in Tables 3 and 4, which show distances between left and right prearicular fiducial landmarks in the original models and after rescaling. The distances after warping match the original C1 model fiducial distance with accuracy better than 1% and about 0.1% in warping A2 to A1.

Table 3. Distance between Fiducial Landmarks for Original Head Models

Model	C1	C2	C3	A1	A2
Distance (cm)	12.24	13.73	14.81	15.88	15.64

Table 4. Distance between Fiducial Landmarks for Warped Head Models

Model	C2	C3'	A1'	A2'
Distance (cm)	12.20	12.12	12.16	15.90

Effect of Head Geometry Mismatch on Source Estimation Accuracy

For this evaluation, a forward projection from a dipole source (near the occipital fontanel) oriented perpendicular to its corresponding cortical patch was generated (Figures 4a and 4b). For all head models used to estimate the source shown in Figure 4a, LFMs were generated using three orthogonal moments for each dipole location ("triples"). For all LFM calculations, the following conductivity values were used based on the average literature values: 0.46 S/m (scalp), 0.018 S/m (skull), 1.79 S/m (CSF), 0.25 S/m (GM), 0.33 S/m (WM).

To investigate the model mismatch effects we compared estimated source solutions obtained from the original model (C1) and the derivative models (C2', C3', and A1'). The MN technique was used to estimate the sources. The metric employed for source localization accuracy in this paper is the localization error distance (LED). The LED is the Euclidean distance between the locations of the true dipole and the dipole with maximum intensity in the source estimation. Smaller LEDs represent more accurate estimates.

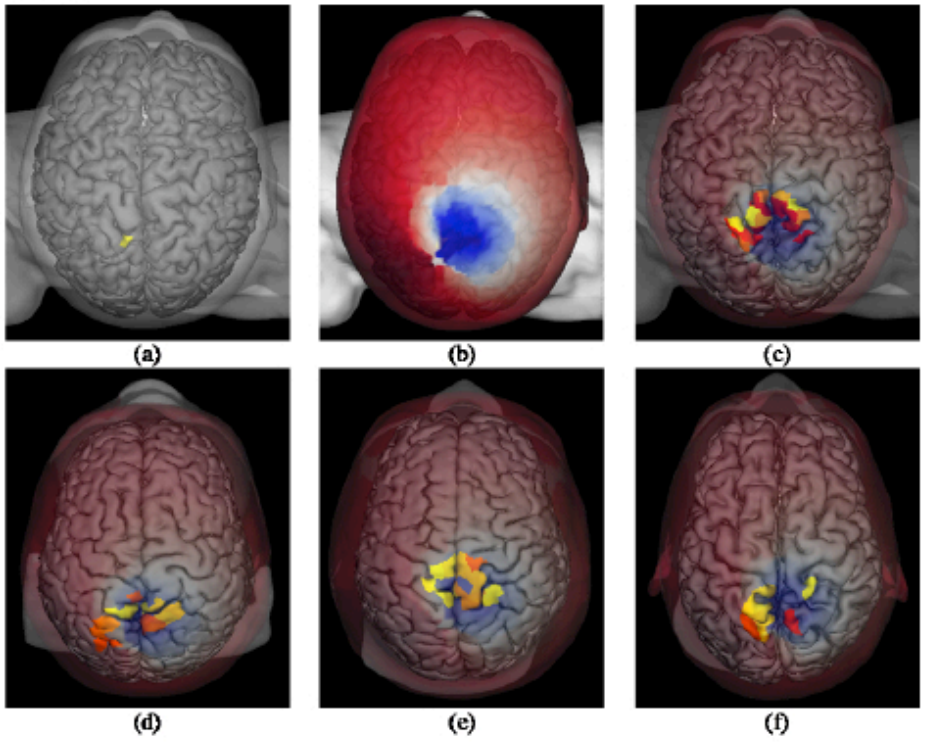

Figure 4. Source estimates as a function of head model. (a) Location of source generator from C1; (b) Forward projection of scalp potential for dipole shown in (a); (c) ESI solution obtained with C1 model; (d) ESI solution obtained with C2' model; (e) ESI solution obtained with C3' model; (f) ESI solution obtained with A1' model.

Table 5. LED of ESI solutions as a function of head geometry

Model	C1	C2'	C3'	A1'
LED	10.5 mm	16.5 mm	15.6 mm	32.7 mm

As shown in Table 5, the LED is minimal when a head model matches the model that generated the scalp potential data. When a subject specific head models are not available, the warped older pediatric group models (C2' and C3') are still reasonable for EEG source localization (LEDs are increasing in this case up to 16 mm). The warped adult model, A1' resulted in the large localization error of ~33 mm.

Effect of Head Model Resolution on Source Estimation Accuracy

The motivation of this study is the fact that an infant head is about twice as small as an adult head and the skull is thinner. Therefore, it is reasonable to expect that a higher resolution model would be required for an infant head to match the same finite difference node density per skull voxel in adults captured by 1 mm resolution images. Another reason is that a current dipole is approximated in FDM as two monopoles at adjacent finite difference grid nodes with the amplitude I (Eq. 1) divided by the voxel volume. Therefore, the overall forward projection will be more accurate for the higher FDM resolution. Resampled subject C1 head volumes were created from the original 1 mm resolution C1 head model. In order to manipulate image resolution of the original head model (.88 mm × .88 mm × .9 mm), each voxel of the post-processed data is either merged with its 6 neighboring voxels or subdivided into 8 separate voxels, thus decreasing and increasing image resolution respectively (Figure 5).

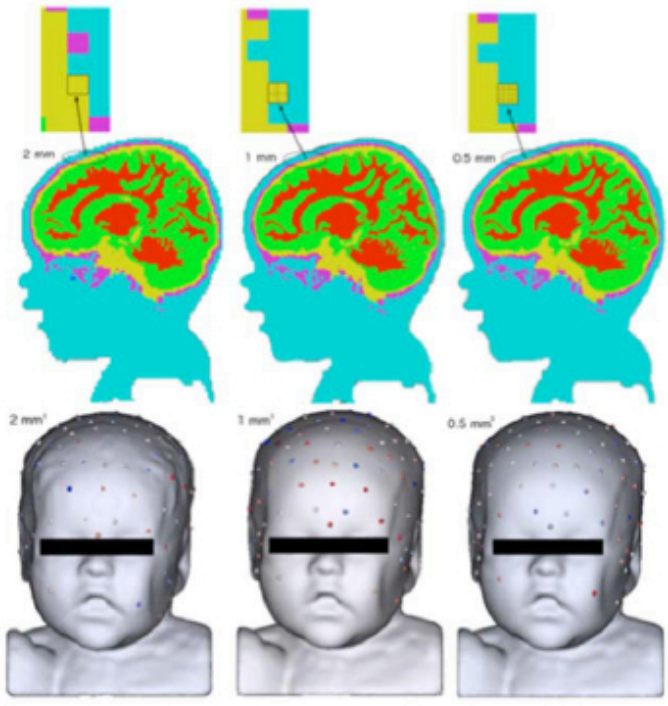

Figure 5. Head models of a 6-month-old infant (C1) at 2 mm (left), 1 mm (center) and 0.5 mm (right) resolutions. Sagittal slices (top), sensors on scalp (bottom).

When decreasing resolution, sets of merged voxels were given a uniform tissue type based on the tissue type that was most common amongst the group before the merge. Due to aliasing, dipoles that were located in WM as a result of voxel merging were automatically deleted and not used for analysis. When increasing resolution, the subdivided voxels were assigned a single tissue type that matches the tissue of the voxel from which they were derived.

Figure 5 shows the effect of the mesh resolution variations for the reference infant model, C1. Sagittal slices show the different FDM grid voxel size of 2 mm^3, 1 mm^3, and 0.5 mm^3. It can be seen in Figure 5 that reduction of resolution to 2 mm leads to visible bumps on the scalp surface (bottom left corner) and disruption in skull morphology (upper left corner sagittal view), as the actual anatomical resolution was decreased in this case along with FDM resolution, while transition from the original 1 mm resolution to the interpolated 0.5 mm resolution simply made FDM grid denser but actually did not improve the original image resolution. In this evaluation, the same 128-sensor positions were registered to all three C1 resolution models. A forward projection for one dipole (Figure 6a) using the 0.5 mm resolution model served as the ground-truth location. The forward projections (lead fields) of this dipole in three resolution cases were calculated and plotted versus sensor number (Figure 6b).

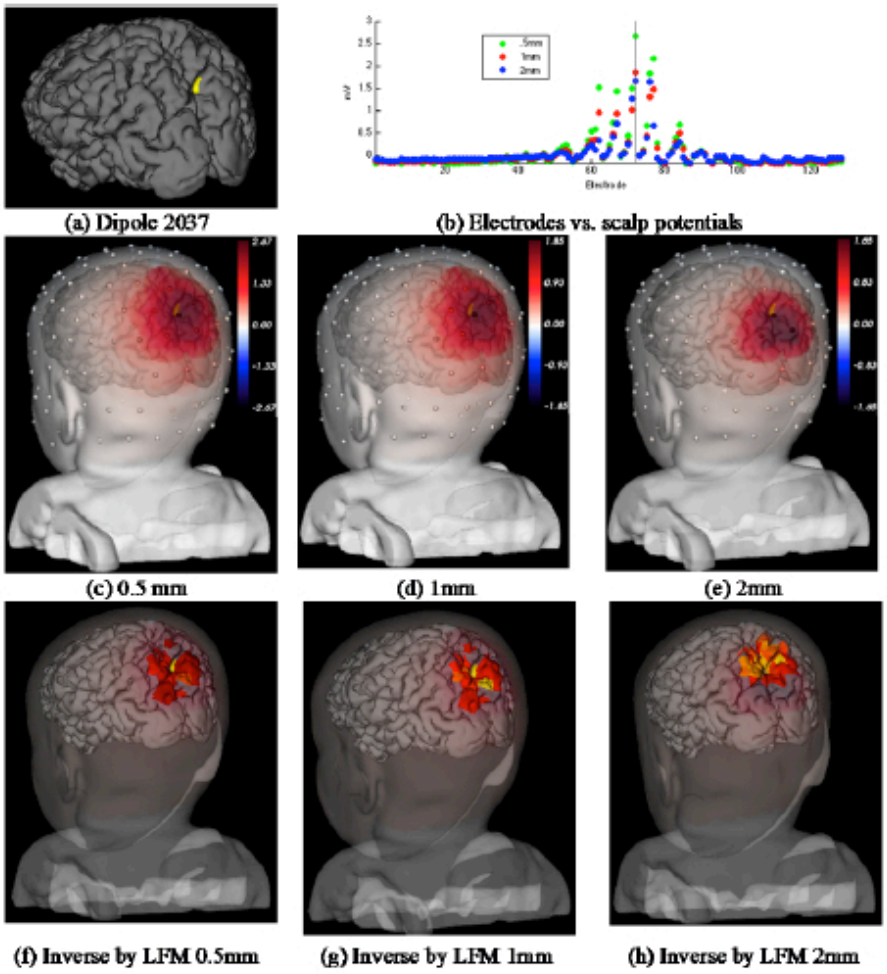

Figure 6. Resolution variation effects on source localization: (a) ground truth dipole location near the occipital fontanel on the cortex; (b) forward projection of potentials to EEG sensors (128 channels) as a function of model resolution; (c-e) 3D views of forward projections to scalp; (f-h) ESI solutions (sLORETA) as a function of model resolution.

One can see that the dipole projection to the scalp is tighter (the full width at half maximum (FWHM) is smaller) for the 0.5 mm resolution, while projections of the same dipole forward fields at 1 mm and 2 mm are more diffused as expected. The ESI solutions (Table 6) using the sLORETA technique derived from the 0.5 mm resolution model correctly localized the dipole (LED is 0 mm, no

resolution mismatch). The source distributions for the lower resolutions are more diffuse, as expected (the error is of 12 mm for this dipole in both mismatched resolutions).

Table 6. LED of ESI solutions as a function of model resolution

Model Resolution	0.5 mm	1 mm	2 mm
LED	0 mm	12.15 mm	11.91 mm

Effect of Tissue Conductivities on Source Estimation Accuracy

To evaluate how inaccurate assumptions of tissue conductivities will impact ESI solutions, LFMs were generated for three different models (C1, A0s, and A1') while varying the skull conductivity (which is the most resistive tissue) across six values (0.004 S/m, 0.018 S/m, 0.1 S/m, 0.2 S/m, 0.35 S/m and 0.45 S/m). This resulted in 18 LFMs. The model with skull conductivity set to 0.1 S/m in each model (assuming that infant bones are more conductive on average than in adults) served as the ground truth. From the ground-truth model, forward projections were generated for each dipole and ESI solutions were derived using MN and sLORETA. The LEDs presented in Table 7 represent the mean LED (i.e., averaged ESI solutions for all dipoles) for each condition.

Table 7. Errors of ESI depending from conductivity and/or model mismatch. The mean LEDs are given in mm. The ground truth LFMs for skull conductivity of 0.1 S/m results in the minimal LED in all three geometries with both MN and sLORETA.

Method	Head Geometry	Skull Conductivity (S/m)					
		0.004	0.018	0.1*	0.2	0.35	0.45
MN	C1	17.25	15.49	15.06	15.12	15.19	15.19
	A0s	18.42	16.22	15.18	15.34	15.39	15.46
	A1'	19.75	18.26	13.97	14.98	16.27	16.63
sLORETA	C1	3.72	0.27	0	0	0	0.003
	A0s	7.63	1.14	0	0	0.017	0.066
	A1'	10.56	4.60	0	0.08	0.54	1.045

As can be seen, LED is minimal for both MN and sLORETA solutions when the conductivity values used in the head model matches with those used to generate the synthetic EEG data. Use of the head models with the correct skull conductivity values results in the minimal LEDs. When skull conductivity is set to be low (skull is more resistive), the LEDs are larger. On the other hand, when skull is effectively replaced bypio soft tissues (conductivity values approaching conductivity of surrounding tissues), the effect is small. The steepest change in LED was observed in the range of conductivities between 0.004 S/m and 0.1 S/m and more pronounced for the rescaled adult head models, A1'.

We believe this is due to the fact that the relative skull thickness of adult model A1, even after rescaling, is larger than in the reference infant model C1, therefore the thicker skull conductivity misspecifications have more impact on the forward solution.

Model Mismatch in SEP experiment

This experimental EEG study was motivated by the need to verify our simulation studies. The expected brain activation regions in SEP experiments are generally well known from human brain anatomy and can be further confirmed by an independent fMRI study (ROI in Figure 7). The dEEG data was processed using Net Station Version 4.5.5 software (Electrical Geodesics, Inc, Eugene, United States). Each subject's data was filtered using a 60 Hz high-pass FIR filter prior to visual bad channel replacement. Manually marked bad channels were replaced using spherical spline interpolation. Data was segmented into 300 ms stimulus-locked epochs from 100 ms prestimulus to 200 ms poststimulus. The ERPs were then averaged and corrected to a 100 ms baseline. Channels contaminated with eye or movement artifacts were identified by a computerized algorithm and were eliminated. Following computerized bad channel replacement, data were mean corrected and referenced to vertex (Cz). ESI using the sLORETA technique was performed on the ~10 ms time window just before the peak of P50 SEP component.

Figure 7 shows the ESI solutions for subject A1 and A2 (sLORETA regularization constant of 0.1). In both subject specific models, clear congruency can be seen in source localization relevance to their predefined anatomical ROI. For subject A2 specifically, the S1 thumb region appears to be functionally defined along the posterior and anterior banks of the postcentral gyrus. In order to demonstrate the importance of head geometry on ESI solutions, we generated a new head model, A2'. This model was applied to the SEP data used for the A2 solution. Figure 7, top right corner shows the results. Notice that the bulk of electrical activity has shifted from the posterior and anterior banks of the postcentral gyrus (S1) to the center of the postcentral gyrus and posterior bank of the precentral gyrus (M1) even though the physical contours of the brain have been unchanged.

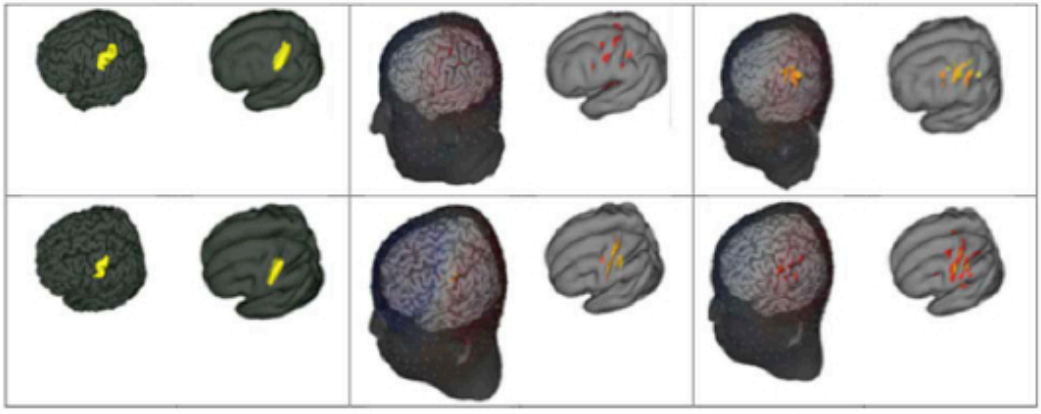

Figure 7. Effects of model mismatch on SEP localization. Top row left to right: subject A2 highlighted anatomical ROI, A2 model specific ESI solution, A2' ESI solution for A2 SEP data (mismatch). Bottom row left to right: A1 highlighted anatomical ROI, A1 model specific ESI solution, A1 ESI solution for A2 SEP data (mismatch).

Finally, we aimed to show what would happen when EEG data is localized to another subject's head model. As can be seen in Figure 7, bottom right corner, EEG data from subject A2 was localized in the individual head model of A1, using the same time point and activity as above. As in the previous mismatch, the bulk of electrical activity has shifted away from the ROI defined for A2, only this time the activity has shifted ventrally (more toward the functional location of subject A1's thumb).

DISCUSSION AND CONCLUSION

The present study demonstrates the importance of accurate physical measurement of head geometry and conductivity for accurate electrical source localization of dense array EEG. Particularly for infants and young children, using rescaled adult electrical head models produces inaccurate results. On the other hand, if the geometry of the child's head is approximated, such as through warping an older child's model to the child's head shape (Figure 4), the source results are a reasonable approximation to what can be gained from using the individual's MRI and CT.

Anatomical data for constructing electrical head models, based on MRI and CT images for a range of age, gender, and ethnicity groups are becoming more readily available [24- 26]. Using these data to create head model atlases with appropriate conductivity specifications is an important near term goal. Given appropriate conductivities, electrical head atlases can be constructed for a look-up repository across the developmental range (from infancy to old age) and across gender and racial groups. To adjust these atlases to a specific subject, a warping procedure to the subject's own head shape (measured noninvasively such as with photogrammetry [36]) can be used and give reasonably accurate results, as suggested by the analyses above.

One approach for gaining accurate head conductivity for each age, sex, and racial group is to use electrical impedance tomography (EIT) for head impedance scanning (impedance is the reciprocal of conductivity). In this approach, harmless currents are injected into the head, and the potential field ("impressed EEG") created by volume conduction of this current through head tissues is measured [1, 14, 27, 28, 34, 35]. From the impressed EEG and the known position of the injected current on the scalp, properties of the head tissue can be inferred through Ohm's law.

Ideally, subject specific electrical models based on native MRIs and CTs structural information and informed with tissue conductivity specifications are the best choice for the most accurate ESI. However, MRIs and CTs are not usually available for many adult subjects and the majority of infants and young children. In such cases, as we have shown on example of pediatric models, one can use a reasonably close by age atlas model and warp it to the subject specific EEG sensor positions cloud (obtained noninvasively with photogrammetry). Adult models rescaled to the infant size are not a good choice due to the far distant morphology (which makes conductivity uncertainties' impact amplified as well), producing as a result localization errors up to 3 cm. We have shown previously [28] that conductivity fitting to experimental impressed EEG is feasible. The actual conductivity values for infant skull are not well known presently, but unlikely to be in the adult range of low values. Therefore further studies are needed for practical noninvasive estimation of head impedance for regional tissue conductivity estimates in infants.

In addition to EEG, there are several other applications for which accurate (preferably subject specific) models of head-shape, tissue boundaries and tissue properties are required. These range from biomechanical models of cranial injury to imaging techniques such as MEG and EIT [1,8,16,28]. With the addition of optical diffusion equations and tissue parameters to the FDM framework, the child head model database can be extended to diffuse optical tomography (DOT) and Near Infrared Spectroscopy (NIRS) [39]. Finally, accurate electrical head models are needed for more accurate interventions, such as with Transcranial Electrical Stimulation (TES) and Transcranial Magnetic Stimulation (TMS) in neurorehabilitation for stroke and TBI patients, treatment of depression and other neurological disorders [17]. Although the specific issues vary in each of these applications, an accurate database of electrical head models could allow neuroimaging and neurointerventional technologies to be extended more accurately to work with children.

ACKNOWLEDGMENTS

This project was supported by the National Institute of Neurological Disorders and Stroke (Grants 5R43NS067726-02 and 5R44NS056758-04).

REFERENCES

[1] Salman A, Turovets S, Malony A., Poolman P, Davey C, Eriksen J, Tucker D. Noninvasive conductivity extraction for high-resolution EEG source localization. *Adv. Clin. Neurosci Rehabil.* 2006;6(1):27-28.

[2] Michel CM, Murray MM, Lantz G, Gonzalez S, Spinelli L, Grave de Peralta R. EEG source imaging. *Clin. Neurophysiol.* 2004;115(10): 2195-2222.

[3] Holmes MD. Dense array EEG: Methodology and new hypothesis on epilepsy syndromes. *Epilepsia*. 2008;49(s3):3-14.

[4] Srinivasan R, Tucker D, Murias M. Estimating the spatial Nyquist of the human EEG. *Behav. Res Methods Instrum Comput*. 1998;30:8–19.

[5] Lantz G, Grave de Peralta R, Spinelli L, Seeck M, Michel CM. Epileptic source localization with high density EEG: how many electrodes are needed? *Clin. Neurophysiol*. 2003;114(1):63-69.

[6] Plummer C, Harvey AS, Cook M. EEG source localization in focal epilepsy: Where are we now? *Epilepsia* 2008;49(2):201-218.

[7] Hallez H, Vanrumste B, Grech R, Muscat J, De Clercq W, Vergult A, D'Asseler Y, Camilleri KP, Fabri SG, Van Huffel S, Lemahieu I. Review on solving the forward problem in EEG source analysis. *J. Neuroeng Rehabil*. 2007;4:46.

[8] Grech R, Cassar T, Muscat J, Camilleri KP, Fabri SG, Zervakis M, Xanthopoulos P, Sakkalis V, Vanrumste B. Review on solving the inverse problem in EEG source analysis. *J. Neuroeng Rehabil.* 2008;5:25. doi:10.1186/1743-0003-5-25.

[9] Knickmeyer RC, Gouttard S, Kang C, Evans D, Wilber K, Smith JK, Hamer RM, Lin W, Gerig G, Gilmore JH. A Structural MRI Study of Human Brain Development from Birth to 2 Years. *J. Neurosci.* 2008;28(47):12176-12182.

[10] Marsh R, Gerber AJ, Peterson BS. Neuroimaging Studies of Normal Brain Development and Their Relevance for Understanding Childhood Neuropsychiatric Disorders. *J. Am. Acad Child Adolesc Psychiatry*. 2008;47(11):1233-1251. doi:10.1097/CHI.0b013e318185e703.

[11] Hammock MK, Mihorat TH. Cranial computed tomography in infancy and childhood. *Other Information: From review in Radiology*. 145(1) (Oct 1982). 1981. Medium: X; Size: Pages: 350.

[12] Neumann K, Moegelin A, Temminghoff M, Radlanski RJ, Langford A, Unger M, Langer R, Bier J. 3D-computed tomography: a new method for the evaluation of fetal cranial morphology. *J. Craniofac Genet Dev Biol*. 1997;17(1):9-22.

[13] Margulies SS, Thibault KL. Infant Skull and Suture Properties: Measurements and Implications for Mechanisms of Pediatric Brain Injury. *J. Biomech Eng*. 2000;122(4):364-371.

[14] Lai Y, van Drongelen W, Ding L, Hecox KE, Towle VL, Frim DM, He B. Estimation of in vivo human brain-to-skull conductivity ratio from simultaneous extra- and intra-cranial electrical potential recordings. *Clin. Neurophysiol*. 2005;116(2):456-465.

[15] Lebel C, Walker L, Leemans A, Phillips L, Beaulieu C. Microstructural maturation of the human brain from childhood to adulthood. *Neuroimage*. 2008;40(3):1044-1055.

[16] van Uitert R, Weinstein D, Johnson C. Volume Currents in Forward and Inverse Magnetoencephalographic Simulations Using Realistic Head Models. *Ann. Biomed Eng*. 2003;31(1):21-31.

[17] Wagner T, Valero-Cabre A, Pascual-Leone A. Noninvasive Human Brain Stimulation. Annu *Rev Biomed Eng*. 2007;9:19.1–19.39. doi: 10.1146/annurev.bioeng.9.061206.133100.

[18] Awada KA, Jackson DR, Baumann SB, Williams JT, Wilton DR, Fink PW, Prasky BR. Effect of conductivity uncertainties and modeling errors on EEG source localization using a 2-D model. *IEEE Trans Biomed Eng*. 1998;45(9):1135-1145.

[19] Vanrumste B, Van Hoey G, Van de Walle R, D'Havé M, Lemahieu I, Boon P. Dipole location errors in electroencephalogram source analysis due to volume conductor model errors. *Med. Biol Eng Comput*. 2000;38(5):528-534.

[20] Pohlmeier R, Buchner H, Knoll G, Rienäcker A, Beckmann R, Pesch J. The influence of skull-conductivity misspecification on inverse source localization in realistically shaped finite element head models. *Brain Topogr*. 1997;9(3):157-162.

[21] Huiskamp G, Vroeijenstijn M, van Dijk R, Wieneke G, van Huffelen AC. The need for correct realistic geometry in the inverse EEG problem. *IEEE Trans Biomed Eng*. 1999;46(11):1281-1287.

[22] Acar ZA, Makeig S. Effects of forward model errors on EEG source localization. *Brain Topogr*. 2013;26(3):378-396.

[23] Roche-Labarbe N, Aarabi A, Kongolo G, Gondry-Jouet C, Dümpelmann M, Grebe R, Wallois F. High-resolution Electroencephalography and source localization in Neonates. *Hum. Brain Mapp*. 2008;29:167-176.

[24] MNI pediatric and adult template head models. Available from: http://www.bic.mni.mcgill.ca/ServicesAtlases/

[25] Fonov V, Evans AC, Botteron K, Almli CR, McKinstry RC, Collins DL; Brain Development Cooperative Group. Unbiased average age-appropriate atlases for pediatric studies. *Neuroimage*. 2011;54:313-327.

[26] Shi F, Yap PT, Wu G, Jia H, Gilmore JH, Lin W, Shen D. Infant brain atlases from neonates to 1- and 2-year-olds. *PLoS ONE*. 2011;6(4);e18746. doi: 10.1371/journal.pone.0018746.

[27] Salman A, Turovets S, Malony A, Volkov V. Multi-cluster, mix-mode computational modeling of human head conductivity. IWOMP 2005/2006. LNCS. 2008;4315:119-130.

[28] Turovets S, Poolman P, Salman A, Malony A, Tucker D. Conductivity analysis for high-resolution EEG. In: Proceedings of 2008 International Conference on Biomedical Engineering and Informatics. *IEEE Computer Society*. 2008;386-393.

[29] Durston S, Casey BJ. What have we learned about cognitive development from neuroimaging? *Neuropsychologia*. 2006;44:2149-2157.

[30] Luna B, Garver KE, Urban TA, Lazar NA, Sweeney JA. Maturation of cognitive processes from late childhood to adulthood. *Child Dev*. 2004;75(5):1357-1372.

[31] Murias M, Swanson JM, Srinivasan R. Functional connectivity of frontal cortex in healthy and ADHD children reflected in EEG coherence. *Cerebral Cortex*. 2007;17:1788-1799.

[32] Li K, Malony A, Tucker DM. Automatic brain MR image segmentation by relative thresholding and morphological image analysis in The First International Conference on Computer Vision Theory and Applications-VISAPP; 2006; Setubal, Portugal.

[33] Li K. BrainK: Structural Image Processing for Electrical Models of the Human Head. *Neuroinformatics*. Forthcoming 2013.

[34] Oostendorp TF, Delbeke J, Stegeman DF. The conductivity of the human skull: Results of in vivo and in vitro measurements. *IEEE Trans Biomed Eng*. 2000;47:1487–1493.

[35] Goncalves SI, de Munck JC, Verbunt JP, Bijma F, Heethaar RM, Lopes da Silva F. In vivo measurement of the brain and skull resistivities using an EIT-based method and realistic models for the head. *IEEE Trans Biomed Eng*. 2003;50(6):754-767.

[36] Russell GS, Eriksen KJ, Poolman P, Luu P, Tucker DM. Geodesic photogrammetry for localizing sensor positions in dense-array EEG. *Clin. Neurophysiol*. 2005;116:1130–1140.

[37] Smith K, Politte D, Reiker G, Nolan TS, Hildebolt C, Mattson C, Tucker D, Prior F, Turovets S, Larson-Prior LJ. Automated measurement of pediatric cranial bone thickness and density from clinical computed tomography. *Conf Proc IEEE Eng Med Biol Soc*. 2012;2012:4462-5. doi: 10.1109/EMBC.2012.6346957.

[38] Walters C. Influence of tissue conductivity and anisotropy on EEG/MEG based source localization in the human brain. PhD Thesis, University of Leipzig, Germany; 2003.

[39] Gibson AP, Hebden JC, Arridge SR. Recent advances in diffuse optical imaging. *Phys Med Biol*. 2005;50(4):R1-R43.

[40] Malony AD, Salman A, Turovets S, Tucker D, Volkov V, Li K, Song JE, Biersdorff S, Davey C, Hoge C, Hammond D. Computational modeling of human head electromagnetics for source localization of milliscale brain dynamics. *Stud. Health Technol Inform*. 2011;163:329-35.

Received: June 17 2013 Revised: June 24 2013 Accepted: June 28 2013